Field-induced spin density wave and spiral phases in a layered antiferromagnet

M. B. Stone,[1] M. D. Lumsden,[1] V. O. Garlea,[1] B. Grenier,[2] E. Ressouche,[2] E. C. Samulon,[3] and I. R. Fisher[3]

[1]*Quantum Condensed Matter Division, Oak Ridge National Laboratory, Oak Ridge, Tennessee 37831, USA*

[2]*INAC-SPSMS, CEA & Université Grenoble Alpes, 38000 Grenoble, France*

[3]*Department of Applied Physics and Geballe Laboratory for Advanced Materials, Stanford University, Stanford, California 94305, USA*

We determine the low-field ordered magnetic phases of the $S = 1$ dimerized antiferromagnet $Ba_3Mn_2O_8$ using single-crystal neutron diffraction. We find that for magnetic fields between $\mu_0 H = 8.80$ T and 10.56 T applied along the $[1\bar{1}0]$ direction the system exhibits spin density wave order with incommensurate wave vectors of type (η, η, ϵ). For $\mu_0 H > 10.56$ T, the magnetic order changes to a spiral phase with incommensurate wave vectors only along the $[hh0]$ direction. For both field-induced ordered phases, the magnetic moments are lying in the plane perpendicular to the field direction. The nature of these two transitions is fundamentally different: the low-field transition is a second-order transition to a spin density wave ground state, while the one at higher field, toward the spiral phase, is of first order.

The mapping of Bose-Einstein condensates and quantum critical points onto the low-temperature magnetic field dependent phase diagrams of quantum antiferromagnets has allowed for further understanding of the exotic ground states and excitations in these systems [1,2]. Although quantum critical points exist purely at zero temperature, their influence can be observed experimentally in these systems at finite temperatures with both thermodynamic and spectroscopic probes [3–5]. Dimerized quantum antiferromagnets have become an especially popular testing ground for such behavior. These systems often consist of strongly coupled spin pairs or dimers with a series of weaker interdimer interactions [6,7]. The system we examine, $Ba_3Mn_2O_8$, has the additional complexity of competing nearest and next-nearest neighbor interactions and of single-ion anisotropy. These effects serve to stabilize an intermediate phase on the magnetic field–temperature phase diagram which has not been observed in other dimer systems.

$Ba_3Mn_2O_8$ is a $S = 1$ antiferromagnet with the Mn^{5+} ions forming a rhombohedral network of weakly coupled dimers. The spin dimers are oriented along the c axis of the hexagonal unit cell as shown in the inset of Fig. 1(a). Interdimer interactions form a frustrated hexagonal network in the ab plane with additional out of plane couplings. Thermodynamic measurements observed a gap in the magnetic excitation spectra of approximately 1 meV [8] with a disordered spin-liquid ground state supporting well defined singlet-triplet excitations. Inelastic neutron scattering measurements have confirmed this and refined the exchange constants illustrated in the inset of Fig. 1(a) [9,10].

Application of a magnetic field along any direction of the crystal structure serves to lift the degeneracy of the triplet excitation into its three S_z components. At $\mu_0 H_{c1} \approx 9$ T, the spin gap is closed and a peak in specific heat and magnetic susceptibility indicates a transition to a magnetically ordered phase [11]. As the magnetic field increases, additional triplet excitations condense into the ground state until $\mu_0 H_{c2} \approx 26$ T where the system reenters a disordered paramagnetic phase. At larger magnetic fields higher order excitations begin to condense into the ground state and a second ordered phase has been found to exist between $\mu_0 H_{c3} \approx 32.5$ and $\mu_0 H_{c4} \approx 47.9$ T [8,12]. Figure 1(a) illustrates the low-temperature phase

diagram in the vicinity of $\mu_0 H_{c1}$. A second phase (phase II) was also found to exist in this region for magnetic fields applied perpendicular to the c axis with critical fields $\mu_0 H_{c1a}$ and $\mu_0 H_{c1b}$ between the quantum paramagnetic phase (QP) and phase II and between phase II and phase I, respectively [13]. For magnetic fields applied along the c axis, only one phase boundary has been observed with thermodynamic measurements (phase I). These two phases have been proposed to be due to the existence of a finite on-site anisotropy term, D, in the Hamiltonian as well as the existence of significant inter-layer exchange interactions along the c axis [14]. The focus of this Rapid Communication is to examine these two phases using neutron diffraction techniques in order to understand their fundamental differences. We find that phase I corresponds to a long-range-ordered spiral phase with an incommensurate wave vector. However the order in phase II is due to a spin density wave, i.e., an amplitude-modulated uniaxial magnetic structure.

Single crystals of $Ba_3Mn_2O_8$ were produced as described in Ref. [11]. Single-crystal magnetic neutron diffraction measurements were performed using the lifting counter two-axis diffractometer D23 at the Institut Laue-Langevin in Grenoble, France. The $m = 0.1$ g sample was mounted in the $(hh\ell)$ scattering plane. This orientation of the sample placed the magnetic field perpendicular to the c axis to access both phases I and II. The sample was mounted within a dilution refrigerator placed within a 12 T vertical field magnet equipped with large vertical access to probe out-of-plane wave vectors with the lifting counter of the diffractometer. Nuclear and magnetic peaks for refinement were measured at a wavelength of $\lambda = 1.2815$ Å using a copper (200) monochromator. Throughout this Rapid Communication, we index reflections using the hexagonal lattice of $Ba_3Mn_2O_8$.

The low-temperature nuclear structure was refined at $\mu_0 H = 12$ T and $T = 0.07$ K using FullProf software [15]. No change in nuclear Bragg peak position or scattering intensity was observed as a function of applied magnetic field. This indicates that the nuclear structure does not change with magnetic field and that the sample remained fixed in position as the magnetic field was varied. The low-temperature high-field structure agrees well with the previously reported structure
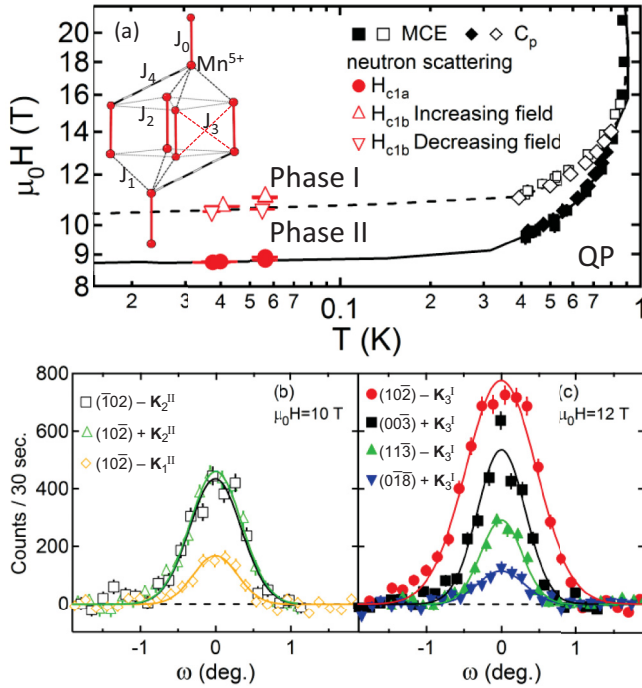
FIG. 1. (Color online) (a) Magnetic field versus temperature phase diagram for $Ba_3Mn_2O_8$ with $\mu_0 H \perp c$. Open and closed black points for $T > 0.3$ K are from the low magnetic field range of Ref. [11], and were determined from magnetocaloric effect (MCE) and heat capacity (C_p) measurements. Points for $T < 0.2$ K correspond to the critical fields observed in neutron scattering measurements (e.g., Fig. 2). Phase boundary lines are guides to the eye. Phase I and phase II are described in the text. Phase QP is a quantum paramagnetic disordered phase. Inset shows the nuclear crystal structure only illustrating the Mn^{5+} $S = 1$ sites. Intradimer (interdimer) exchange is depicted with solid (dashed) lines with labeling of exchange paths as in Ref. [10]. (b) Rocking curves of magnetic Bragg peaks at $\mu_0 H = 10$ T. (c) Rocking curves of magnetic Bragg peaks at $\mu_0 H = 12$ T. Rocking curves have been offset by their peak location in ω, the sample rotation angle, such that they are centered at $\omega = 0$. Rocking curves have been offset vertically by their fitted background value. Solid lines through rocking curves are Gaussian fits. The scattering vectors of the individual rocking curves are listed in the figure caption.

at ambient temperature [16]. A summary of the nuclear refinement is discussed in the Supplemental Material [17].

A search in reciprocal space to find magnetic ordering wave vectors was made in the vicinity of $(\frac{m}{3}, \frac{n}{3}, \ell)$ for integer m and n. These wave vectors are near the location of the overall minimum in the singlet-triplet dispersion [10]. In an applied magnetic field, the spin gap will close first very close to these wave vectors. Broad scans along $(\frac{m}{3}, \frac{n}{3}, \ell)$ directions for fixed integer values of m and n were performed using a graphite monochromator and relaxed instrument collimation to improve the measured scattering intensity. Once individual magnetic Bragg peaks were observed, their positions were further refined by using the copper monochromator with additional beam collimation.

Figure 1(b) shows several characteristic magnetic Bragg peaks for $\mu_0 H = 10$ T. The determined peak positions were

found to be incommensurate with the crystal lattice both in the a^*-b^* plane and along the c^* direction. We characterized the propagation vectors as $\mathbf{k} = (\eta, \eta, \epsilon)$ with $\eta_{II} = 0.316 \pm 0.01$ and $\epsilon_{II} = 0.04 \pm 0.009$ from reciprocal space scans in phase II [18]. There are six potential propagation vectors of the type $\mathbf{k} = (\eta, \eta, \epsilon)$ for the $R\bar{3}m$ space group [17]. The six *arms* of the $\mathbf{k} = (\eta, \eta, \epsilon)$ *star* are $\mathbf{k}_1 = (\eta, -2\eta, \epsilon)$, $\mathbf{k}_2 = (-2\eta, \eta, \epsilon)$, $\mathbf{k}_3 = (\eta, \eta, \epsilon)$, $\mathbf{k}_4 = (\eta, -2\eta, -\epsilon)$, $\mathbf{k}_5 = (-2\eta, \eta, -\epsilon)$, $\mathbf{k}_6 = (\eta, \eta, -\epsilon)$. An extensive search in reciprocal space at $\mu_0 H = 10$ T found magnetic reflections for only two of these propagation vectors which we label as $\mathbf{k}_1^{II} = (\eta_{II}, -2\eta_{II}, \epsilon)$ and $\mathbf{k}_2^{II} = (-2\eta_{II}, \eta_{II}, \epsilon)$. The other potential propagation vectors for the $R\bar{3}m$ space group were examined, but found to not have any magnetic scattering intensity. Both the $\mathbf{k}_1^{II}$ and $\mathbf{k}_2^{II}$ vectors are approximately $\pm 30°$ from the applied magnetic field direction. A small misalignment of the magnetic field relative to the crystallographic axes may be favoring these domains over the $\mathbf{k}_3^{II} - \mathbf{k}_6^{II}$ domains. The value of η_{II} agrees well with the location of the minimum in the zero-field magnon dispersion. The incommensurability along the c^* axis is small but nonzero, and is a likely consequence of a small next-nearest-neighbor bilayer exchange coupling in the system that has not been accounted for in prior models of $Ba_3Mn_2O_8$.

For $\mu_0 H = 12$ T, we observe a single incommensurate propagation vector with greater overall intensity than that found for either of the two propagation vectors in phase II. The incommensurability along the c^* axis vanishes, $\epsilon_I = 0 \pm 0.009$, and the incommensurability in the plane shifts slightly $\eta_I = 0.313 \pm 0.01$. There are three potential propagation vectors of the type $\mathbf{k} = (\eta, \eta, 0)$ for the $R\bar{3}m$ space group [17]. An extensive search in reciprocal space at $\mu_0 H = 12$ T found magnetic reflections only for propagation vectors of the type $\mathbf{k}_3^I = (\eta_I, \eta_I, 0)$. The equivalent propagation wave vectors were examined and found not to exist. The magnetic Bragg peak locations observed in phase I are at wave vectors very near the minima of the zero-field dispersion of $Ba_3Mn_2O_8$ just as in phase II. However, the ordered state of phase I is not the same as that of phase II.

Figure 2 illustrates the magnetic field dependence of a magnetic Bragg peak in each of the phases. These measurements were performed by counting for a fixed number of incident neutrons on a beam monitor while the magnetic field was slowly increased or decreased. No heating of the sample was observed during this process. The temperature for these measurements was fixed between 0.04 and 0.06 K. The rate of the changing magnetic field was doubled for one of the measurements without any discernible change in the resulting data. There is no hysteresis observed between phase II and the quantum paramagnetic phase, suggesting a second-order phase transition. However there is hysteresis in crossing between phase II and phase I for measurements of Bragg peaks of both these phases suggesting either a first-order transition or a spin-glass system not in equilibrium at this phase boundary. We do not anticipate this transition to be associated with a glassy state due to the lack of such effects observed in extensive thermodynamic measurements. Nuclear reflections were also examined as a function of applied magnetic field. Within the counting statistics of the experiment, the peak intensity and location of nuclear reflections were found to remain constant with field.
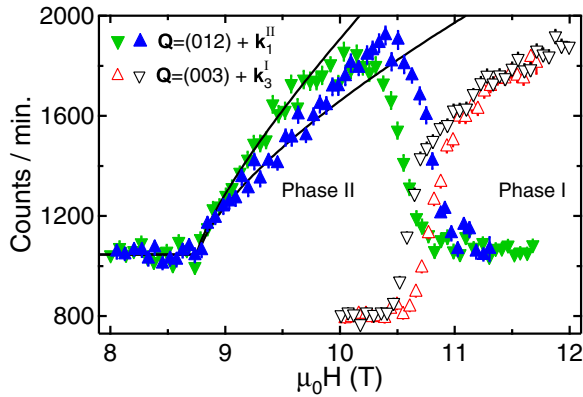
FIG. 2. (Color online) Intensity as a function of magnetic field for two magnetic Bragg peaks corresponding to the two low-temperature ($T \approx 0.05$ K) magnetic phases in $Ba_3Mn_2O_8$. Vertical triangle symbols correspond to increasing the magnetic field; inverted triangle symbols correspond to decreasing the applied magnetic field during the measurement. Solid lines are fits to a power law for a range of 1 T above the critical field for each measurement. Extracted order parameter values are discussed in the text.

The neutron scattering magnetic cross section allows one to extract information regarding the order parameter β associated with the sublattice magnetization. We fit the field-dependent magnetic scattering in the vicinity of 8.75 T to a power law of the form $I = I_0 + A(H - H_c)^{\beta}$ for $H > H_c$ and $I = I_0$ for $H \leqslant H_c$ where I_0 is an overall background above and below the critical field H_c. We fit over the range of data up to 1 T greater than the critical field. To determine an appropriate error bar for the extracted values of β, we also perform separate fits for a range of $H_c + dH$ for $dH = 0.5$ and 1.5 T. The determined critical field values are plotted in Fig. 1(a), and are consistent with the higher temperature values obtained from thermodynamic measurements. Low-temperature individual rocking curves were also performed as a function of applied magnetic field for the ordering wave vector in phase II. The extracted critical fields for these measurements are the low-temperature values plotted in the phase diagram. We parametrize the transition into phase I with the power-law expression to extract a reasonable value of H_c. Because this is likely a first-order transition, it is not appropriate to extract an order parameter.

The order parameter and critical field determined for increasing the magnetic field through the QP to phase II transition is $\beta = 0.35^{+0.09}_{-0.07}$ with $\mu_0 H_{c1a} = 8.77(2)$ T. Very similar values are found for decreasing the magnetic field through this transition: $\beta = 0.39^{+0.07}_{-0.06}$ with $\mu_0 H_{c1a} = 8.75(2)$ T [18]. These values agree with a three-dimensional description of the transition. Calculated values of β for the Heisenberg, XY, and Ising models all potentially agree with our measured values [19–21]. High point density thermodynamic measurements in the vicinity of this transition would serve to further limit this classification.

The magnetic reflections were normalized to the scattering intensity found from the nuclear refinement [15]. Phase II was modeled assuming the existence of two magnetic domains with propagation vectors $\mathbf{k}_1^{II}$ and $\mathbf{k}_2^{II}$ as described earlier.

Refinements were performed using 31 reflections from one domain and 37 magnetic reflections from the second domain. We note that a domain structure and a multi-$\mathbf{k}$ structure (where $\mathbf{k}_n$ coexist) cannot be distinguished from our data, so that the latter possibility cannot be ruled out. The refined magnetic structure for phase II is a spin density wave (SDW) with the spins always pointing within the plane defined by the c axis and the [110] direction, perpendicular to the applied magnetic field. A phase angle was allowed to vary between the projected moments of the Mn sites $(0,0,z)$ and $(0,0,\bar{z})$, This phase converged to nearly $180°$, consistent with antiferromagnetic dimers. Assuming the magnitude of the moment to be identical for both domains, we arrived at a value of 1.4(1) μ_B with a canting angle magnitude of 22.4 ± 3.5 degrees with respect to the c axis and domain populations of 52% and 48% for domain $\mathbf{k}_1^{II}$ and $\mathbf{k}_2^{II}$, respectively [17]. Figure 3(a) is an illustration of the magnetic order determined for one of the wave vector pairs in phase II. Considering the proposed effective Dzyaloshinskii-Moriya (DM) interaction between dimer pairs in the staggered adjacent layers [13], one can also consider a model that combines the two pairs of $\mathbf{k}$'s into a single domain 2-$\mathbf{k}$ magnetic structure. In this scenario, the canting angle alternates from one dimer layer to the next. This model would be in better agreement with magnetometry measurements [11,13] which indicated an axial anisotropy along the c axis. This potential 2-$\mathbf{k}$ model is illustrated in Fig. 3(b).

We modeled the high-field phase using 70 measured reflections and the single propagation vector $\pm\mathbf{k}_3^I$. The best description of the data was obtained by using a spiral (cycloid) magnetic structure rather than a spin density wave. The spiral structure exhibits a nearly perfect circular orbit with the magnitude of the magnetic moment being 0.78(3) μ_B. This value compares well to the moment of phase II considering the average moment of the SDW would be $\frac{2}{\pi}$ times the refined amplitude of the SDW. The moments all lie within the plane defined by the c axis and the [110] direction, perpendicular to the applied magnetic field. The moments are collinear for neighboring spins along the **b-a** direction. The moments for each particular spin pair point $180°$ apart. Figure 3(c) is an illustration of the magnetic order determined for phase I. Additional information regarding the magnetic structural refinement of both phases is given in the Supplemental Information [17]. We also note that with magnetic fields just above $\mu_0 H_{c1}$ these measurements are not sensitive to small ferromagnetic components of the ordered magnetic structures. As the magnetic field increases up to $\mu_0 H_{c2}$, there will be a growing ferromagnetic moment as one reenters the paramagnetic half-magnetized phase.

Through low-temperature high magnetic field neutron diffraction measurements we are able to determine the nature of the proposed ordered phases in $Ba_3Mn_2O_8$. We indeed observe magnetic order consistent with predictions based upon the established Hamiltonian for $Ba_3Mn_2O_8$; i.e., phase II is an Ising-like amplitude-modulated phase and phase I is an incommensurate spiral structure [11]. Low-temperature NMR measurements as a function of magnitude and direction of applied magnetic field have found that for $H \perp \mathbf{c}$, as in our measurement, the transition between the quantum paramagnet
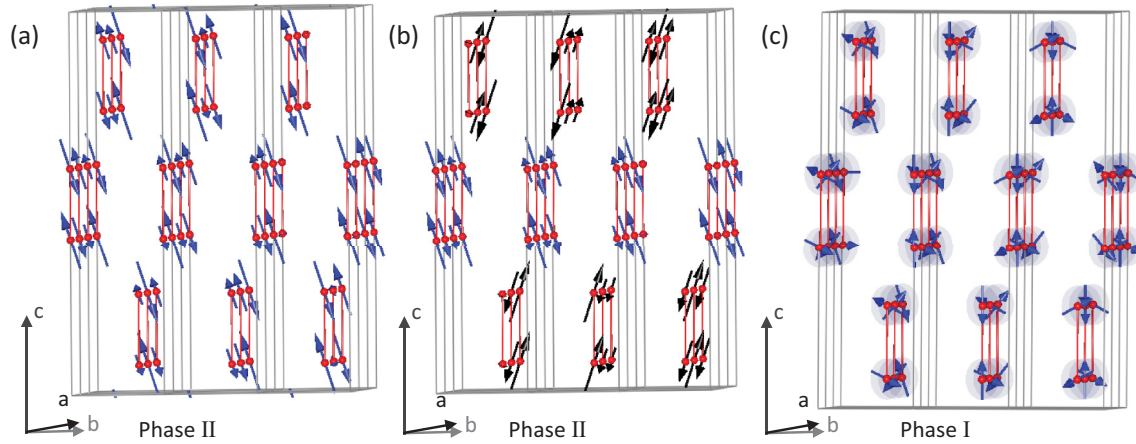
FIG. 3. (Color online) (a) Ordered magnetic structure as determined for $\mu_0 H = 10$ T, phase II. Structure corresponds to domain $\mathbf{k}_1^{II}$. (b) 2-$\mathbf{k}$ magnetic structure scenario for phase II with different colored spin vectors representing the alternating canting angle along the c axis. (c) Ordered magnetic structure, $\mathbf{k}_3^I$, as determined for $\mu_0 H = 12$ T. Only the Mn^{5+} sites with the ordered spin vector are shown in the figures for clarity. The vertical axis of the figures corresponds to the crystallographic c axis. The spins lie in the plane perpendicular to the direction of the applied magnetic field ($H \parallel [1\bar{1}0]$). Gray lines are the boundaries of unit cells. Red lines between Mn^{5+} sites are shown to illustrate the dimers. Blue and black vectors are the directions of the $S = 1$ moments. Blue shaded disks in (c) illustrate the cycloid structure. Measurements were performed in the $[hh\ell]$ scattering plane with the magnetic field perpendicular to this plane. The direction of the magnetic field is approximately normal to the page.

phase and the ordered phase is more Ising-like instead of being defined by the Bose-Einstein quantum critical point for $H \parallel c$ [14]. The order parameter we determine for the transition between phase II and the quantum paramagnetic phase agrees with this. Recent large-size cluster mean-field models have determined that the hysteretic response we observe between phase I and phase II may in fact be a general feature of quasi-two-dimensional triangular lattice dimerized antiferromagnets [22]. This makes Ba$_3$Mn$_2$O$_8$ the first such system in which this effect has been observed and may make this system a candidate for exhibiting so-called magnon or spin supersolid behavior [23]. The dimerized nature of the interactions as well as the existence of frustrated interdimer coupling is also likely contributing to this behavior in Ba$_3$Mn$_2$O$_8$ [24].

[1] T. Giamarchi, C. Rüegg, and O. Tchernyshyov, Nat. Phys. **4**, 198 (2008).

[2] V. Zapf, M. Jaime, and C. D. Batista, Rev. Mod. Phys. **86**, 563 (2014).

[3] S. E. Sebastian, N. Harrison, C. D. Batista, L. Balicas, M. Jaime, P. A. Sharma, N. Kawashima, and I. R. Fisher, Nature (London) **441**, 617 (2006).

[4] Ch. Rüegg, N. Cavadini, A. Furrer, H.-U. Güdel, K. Krämer, H. Mutka, A. Wildes, K. Habicht, and P. Vorderwisch, Nature (London) **423**, 62 (2003).

[5] A. K. Bera, B. Lake, A. T. M. N. Islam, B. Klemke, E. Faulhaber, and J. M. Law, Phys. Rev. B **87**, 224423 (2013).

[6] M. B. Stone, Y. Chen, D. H. Reich, C. Broholm, G. Xu, J. R. D. Copley, and J. C. Cook, Phys. Rev. B **90**, 094419 (2014).

[7] M. B. Stone, I. Zaliznyak, D. H. Reich, and C. Broholm, Phys. Rev. B. **64**, 144405 (2001).

[8] M. Uchida, H. Tanaka, H. Mitamura, F. Ishikawa, and T. Goto, Phys. Rev. B **66**, 054429 (2002).

[9] M. B. Stone, M. D. Lumsden, Y. Qiu, E. C. Samulon, C. D. Batista, and I. R. Fisher, Phys. Rev. B **77**, 134406 (2008).

[10] M. B. Stone, M. D. Lumsden, S. Chang, E. C. Samulon, C. D. Batista, and I. R. Fisher, Phys. Rev. Lett. **100**, 237201 (2008).

[11] E. C. Samulon, Y.-J. Jo, P. Sengupta, C. D. Batista, M. Jaime, L. Balicas, and I. R. Fisher, Phys. Rev. B **77**, 214441 (2008).

[12] E. C. Samulon, Y. Kohama, R. D. McDonald, M. C. Shapiro, K. A. Al-Hassanieh, C. D. Batista, M. Jaime, and I. R. Fisher, Phys. Rev. Lett. **103**, 047202 (2009).

[13] E. C. Samulon, K. A. Al-Hassanieh, Y.-J. Jo, M. C. Shapiro, L. Balicas, C. D. Batista, and I. R. Fisher, Phys. Rev. B **81**, 104421 (2010).

[14] S. Suh, K. A. Al-Hassanieh, E. C. Samulon, I. R. Fisher, S. E. Brown, and C. D. Batista, Phys. Rev. B **84**, 054413 (2011).

[15] J. Rodriguez-Carvajal, Physica B **192**, 55 (1993); program available at http://www.ill.eu/sites/fullprof.

[16] M. T. Weller and S. J. Skinner, Acta Crystallogr., Sect. C: Cryst. Struct. Commun. **55**, 154 (1999).

[17] See Supplemental Material at http://link.aps.org/supplemental/10.1103/PhysRevB.92.020415 for a refined atomic crystal structure parameters and further details regarding the magnetic structure refinement.

[18] Values in parentheses and in $\pm$ superscripts or subscripts correspond to an error of one standard deviation.

[19] M. Campostrini, M. Hasenbusch, A. Pelissetto, P. Rossi, and E. Vicari, Phys. Rev. B **65**, 144520 (2002).

[20] M. Campostrini, M. Hasenbusch, A. Pelissetto, P. Rossi, and E. Vicari, Phys. Rev. B **63**, 214503 (2001).

[21] M. Campostrini, A. Pelissetto, P. Rossi, and E. Vicari, Phys. Rev. E **60**, 3526 (1999).

[22] D. Yamamoto and I. Danshita, Phys. Rev. B **88**, 014419 (2013).

[23] E. Kim and M. H. W. Chan, Nature (London) **427**, 225 (2004).

[24] P. Sengupta and C. D. Batista, Phys. Rev. Lett. **98**, 227201 (2007).